Experiments in Fluids manuscript No.
(will be inserted by the editor)

Quantification of the effect of surface heating on shock wave modification by a plasma actuator in a low density supersonic flow over a flat plate

Romain Joussot · Viviana Lago · Jean-Denis Parisse

Received: date / Accepted: date

Abstract This paper describes experimental and numerical investigations focused on the shock wave modification induced by a dc glow discharge. The model is a flat plate in a Mach 2 air flow, equipped with a plasma actuator composed of two electrodes. A weakly ionized plasma was created above the plate by generating a glow discharge with a negative dc potential applied to the upstream electrode. The natural flow exhibited a shock wave with a hyperbolic shape. Pitot measurements and ICCD images of the modified flow revealed that when the discharge was ignited, the shock wave angle increased with the discharge current. The spatial distribution of the surface temperature was measured with an IR camera. The surface temperature increased with the current, and decreased along the model. The temperature distribution was reproduced experimentally by placing a heating element instead of the active electrode, and numerically by modifying the boundary condition at the model surface. For the same surface temperature, experimental investigations showed that the shock wave angle was lower than for the case with the discharge switched on. The results show that surface heating is responsible for roughly 50% of the shock wave angle increase, meaning that purely plasma effects must also be considered to fully explain the flow modifications observed.

R. Joussot · V. Lago
ICARE, CNRS, UPR 3021
1C Avenue de la Recherche Scientifique, 45071, Orléans Cedex 2, France
E-mail: romain.joussot@cnrs-orleans.fr
E-mail: viviana.lago@cnrs-orleans.fr

J.-D. Parisse
IUSTI, Aix Marseille Université / CNRS, UMR 7343
5 rue Enrico Fermi, Technopôle Château-Gombert, 13453, Marseille Cedex 13, France
E-mail: jean-denis.parisse@univ-amu.fr

1 Introduction

Over the past two decades, there has been considerable research into the use of plasma-based devices in flow-control applications (i.e. plasma actuators), both numerically and experimentally. Many flow regimes are concerned, from low-speed subsonic airflow to hypersonic flow, including moderate-velocity subsonic, transonic, and supersonic flows. Several reviews are available for high speed flow regimes and testify to the considerable research effort into active flow control research using plasma actuators. For instance, one can refer to the work of Fomin et al (2004); Bletzinger et al (2005); Leonov (2011); Wang et al (2012).

Plasma actuators are extensively deployed for flow control applications because of their ability to achieve flow actuation with a high-bandwidth ($\mathscr{O}(\mathrm{Hz}-\mathrm{kHz})$) and without moving mechanical parts. From a general point of view, a plasma actuator is a simple electrical device based on the use of a gas discharge. As many types of discharge are potentially usable (Raizer, 1991), a wide variety of different types of plasma actuators has been studied in the literature. Among the ones most commonly used are those based on a surface dielectric barrier discharge (dbd) with linear (Roth, 2003) or serrated electrode design (Joussot et al, 2013), surface dbd with multiple electrodes (Benard et al, 2009), surface direct current (dc) (Shang et al, 2008), bulk dc glow discharge (Menier et al, 2007), dc filamentary discharge (Leonov and Yarantsev, 2008), arc discharge (Gnemmi and Rey, 2009), radio frequency discharge (Dedrick et al, 2011), and corona discharge (Artana et al, 2002), for instance. The main limitation in using a particular type of plasma actuator is often driven by the flow conditions, especially by the pressure condition. In rarefied flow regimes, corona and glow discharges are mainly used as this regime implies low pressures, except in the case of micro-fluidic studies where rarefaction effects are due to the small dimensions. Plasma ac-

tuators based on other types of discharge (for instance, surface dc discharge, dbd, or arc discharge) are scarcely ever used owing to their working limitation imposed by the discharge physics itself. In the case of a low pressure, the free mean path is too large in comparison to the actuator dimensions to use these types of plasma actuators.

Flow control research in the compressible regime plays a major role in many applications such as aerospace, defense and transportation. Under supersonic flow conditions, thermal effects, including surface and bulk (i.e., gas) heating, are commonly interpreted as the main physical mechanisms responsible for aerodynamic effects resulting from electrical discharges created in the air flow (Semenov et al, 2002; Bletzinger et al, 2005). While many experimental studies have been undertaken at high speed flows, the interpretation of some of the experimental results remains problematic (Bityurin and Klimov, 2005; Shin et al, 2007), especially for experiments in which a change in the discharge polarity leads to different aerodynamic effects (Bityurin and Klimov, 2005; Shin et al, 2007). In high speed flow control, quantification of the non-thermal mechanisms is very important for future applications but also very difficult to conduct because these mechanisms act in addition to thermal effects, which can overshadow non-thermal effects (Macheret et al, 2004; Shang et al, 2008). Analysis of the investigations carried out to date highlights the fact that the results of many studies are attributed to purely thermal effects. In such cases, the flow modifications are due to thermal mechanisms of interaction coming from the energy release of the discharge. However, when the ionization rate is relatively high ($> 10^{-5}$, Macheret et al (2004)), other types of effects must be considered to explain the observed flow modifications (Lago et al, 2014). It is still not clear, however, what the nature of these effects is: bulk heating, purely plasma effects (i.e., ionization or thermal disequilibrium), etc.

This paper combines experiments and numerical simulations in order to gain a better understanding of the surface heating occurring when a plasma discharge is used to modify the flow around a flat plate. This study follows previous work presented in Menier et al (2007); Parisse et al (2009), but presents a significant improvement in that the temperature gradient over the flat plate is taken into account both experimentally and numerically. While evidence for the thermal nature of the interaction between the flow and the plasma discharge is overwhelming, the present study gives rise to a quantification of the surface heating and hence shows that a purely plasma effect has also to be considered to explain the observed flow modifications.

2 Experimental setup

2.1 The MARHy wind tunnel

The MARHy low density facility of the ICARE laboratory (CNRS, France) is used for both academic and industrial research. The wind tunnel was built in 1963, and until 2006 'MARHy' was known as the 'SR3' wind tunnel of the 'Laboratoire d'Aérothermique' (former name of ICARE). A schematic view of the facility is presented in Fig. 1. It consists of three main parts: the settling chamber with a diameter of 1.3 m and a length of 2.0 m, the test chamber with a diameter of 2.3 m and a length of 5.0 m, and a third chamber in which a diffuser is installed. The diffuser is connected to the pumping group by a vacuum gate. A powerful pumping group with 2 primary pumps, 2 intermediary Roots blowers and 12 Roots blowers ensures the low density flow conditions in continuous operating mode. Depending on the desired rarefaction level, the number of pumps used can be varied. When supplied with different nozzles, the wind tunnel generates subsonic, supersonic and hypersonic flows from Mach 0.8 to Mach 21, and covers a large range of Reynolds numbers from 10^2 up to 10^5, for a reference length of 10 cm. The present study was carried out with a Mach 2 contoured nozzle, giving a uniform flow distribution through the test section with a core of 12 cm in diameter (Parisse et al, 2009). The nominal operating conditions, detailed in Tab. 1, are: 63 Pa for the stagnation pressure and 8 Pa for the static pressure of the test section, corresponding to a geometric altitude of 67 km. The subscripts $_0$ and $_1$ stand for the stagnation condition and the free stream one, respectively. In Tab. 1, the pressures p_0 and p_1, and the air temperatures T_0 and T_1 were measured. The other parameters are computed from these values. The Mach number M_1 of the gas flowing out of the nozzle was calculated with the following relation:

$$M_1^2 = \frac{2}{\gamma - 1}\left[\left(\frac{p_0}{p_1}\right)^{\frac{\gamma-1}{\gamma}} - 1\right], \tag{1}$$

where p_0 is the stagnation pressure, p_1 is the static pressure of the test section, and γ is the isentropic exponent of the flow (for unionized air, $\gamma = 1.4$).

2.2 Flat plate and actuators

The model under investigation is a flat plate (100 mm long, 80 mm wide, and 4 mm thick) made of quartz, with a sharp leading edge (15°). The flat plate is mounted in the test section, 174 mm downstream the nozzle exit (see Fig. 2). The Reynolds number ($Re_L = U_1 L/\nu_1$) based on the flat plate length L and calculated with the experimental inflow conditions (see Tab. 1) is $Re_L = 794$. The Knudsen number

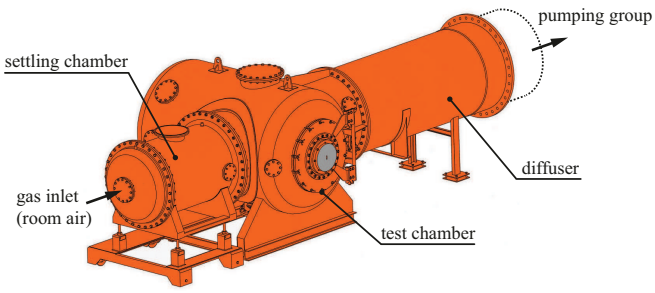

Fig. 1 Schematic view of the MARHy wind tunnel without the pumping group.

Table 1 Operating conditions.

Stagnation conditions	Free stream conditions
$p_0 = 63\,\mathrm{Pa}$	$p_1 = 8\,\mathrm{Pa}$
$T_0 = 293\,\mathrm{K}$	$T_1 = 163\,\mathrm{K}$
$\rho_0 = 7.44 \times 10^{-4}\,\mathrm{kg{\cdot}m^{-3}}$	$\rho_1 = 1.71 \times 10^{-4}\,\mathrm{kg{\cdot}m^{-3}}$
	$\mu_1 = 1.10 \times 10^{-5}\,\mathrm{Pa{\cdot}s}$
	$U_1 = 511\,\mathrm{m{\cdot}s^{-1}}$
	$M_1 = 2$
	$\lambda_1 = 0.375\,\mathrm{mm}$
	$q_m = 3.34 \times 10^{-3}\,\mathrm{kg{\cdot}s^{-1}}$

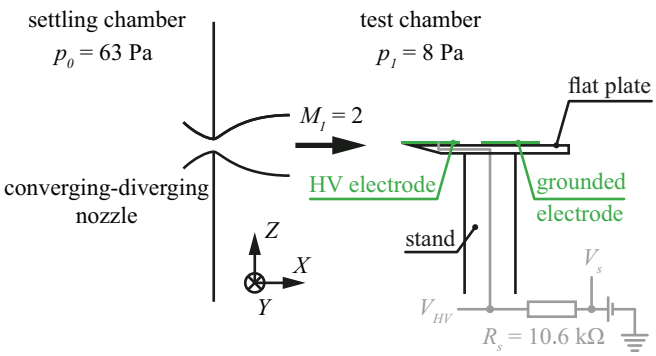

Fig. 2 Schematic view of the flat plate in the case of the plasma actuator.

($Kn_L = \lambda_1/L$) based on the same experimental conditions is $Kn_L = 0.004$, corresponding to the slip-flow regime or slightly rarefied regime.

The plasma actuator is composed of two aluminum electrodes (80 mm long, 35 mm wide, 80 µm thick), which are flush mounted on the upper surface of the flat plate (see Fig. 3a). The first electrode, called the active electrode, is set at the leading edge of the plate and is connected to a high voltage dc power supply (Spellman, SR15PN6) through a resistor ($R_s = 10.6\,\mathrm{k\Omega}$), while the second one is grounded. The glow discharge is generated by applying a negative dc potential to the active electrode, acting as a cathode. The high voltage V_s is fixed with the power supply, which delivers the discharge current I_{HV}. The voltage applied to the active electrode, V_{HV}, is then calculated with the following relation: $V_{HV} = V_s - R_s I_{HV}$. The discharge is ignited in air.

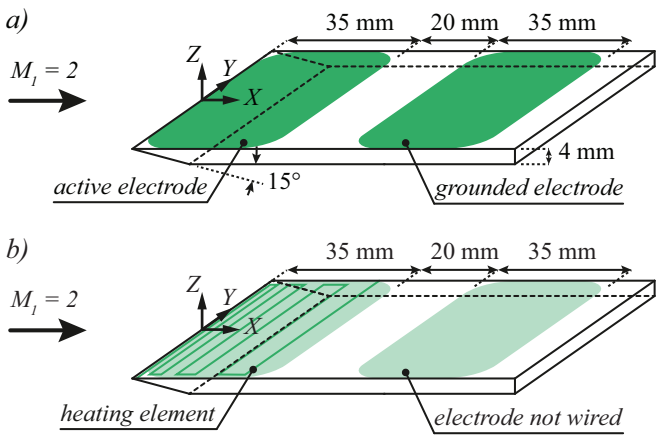

Fig. 3 Schematic views of the flat plate with: *(a)* the plasma actuator and *(b)* the heating element.

A heating element was designed and built to reproduce a similar surface heating than that measured with the plasma actuator. The heating actuator, namely the heater, is composed of a 0.15 mm-diameter resistance wire ($28\,\Omega{\cdot}\mathrm{m}^{-1}$, Cu-Ni-Mn alloy, ISOTAN®) embedded between two layers of polyimide film. The heater is flush mounted on the flat plate surface instead of the active electrode (see Fig. 3b). In order to preserve the same flow topology as that of the plasma actuator, the grounded electrode is present on the surface plate, but not wired. Special attention was applied to reproduce with the heater actuator the same temperature distributions profile than those measured with the plasma actuator (see Sect. 4.1). For this purpose, the spatial distribution of the resistance wire along the X-direction was not uniform. While the longitudinal profile of the surface temperature depends exclusively on the distribution of resistive wires into the heater, the maximum value of the surface temperature which could be reached depends on the current value applied to the heater. The heater was connected to a dc power supply (0–60 V, 0–2.5 A).

2.3 Average flow field measurement diagnostics

2.3.1 Pressure measurement

The stagnation pressure p_0 and test section pressure p_1 were measured with two MKS Baratron capacitance manometers (Type 627D) with 0-10 Torr and 0-0.1 Torr ranges, respectively. Both manometers are connected to a MKS control unit (PR 4000B) with a 12-bit resolution. According to the information provided by the manufacturer, the 0-10 Torr (0-0.1 Torr) pressure transducer has a signal accuracy of $\Delta p_0^{acc} = \pm 0.12\%$ ($\Delta p_1^{acc} = \pm 0.15\%$) of the reading, and a time response below 20 ms (40 ms). The pressure in the flow above the plate was measured with a Pitot probe connected to a

MKS Baratron capacitance manometer (Type 626A, 0-1 Torr) connected to a MKS control unit (PDR-C-2C). The manufacturer's stated accuracy of the transducer signal was $\Delta p^{acc}_{Pitot} = \pm 0.25\%$ of the reading. All the transducers were calibrated in the laboratory and shown to be linear within $\Delta p^{lin} = \pm 0.2\%$. The total uncertainty of the pressure measurements is given in Sect. 2.3.4. A 3-axis traversing system, controlled by a computer, ensured the displacement of the Pitot probe with a step resolution on each axis of $0.1\,\mathrm{mm} \pm 0.02\,\mathrm{mm}$ on each position.

The Pitot probe was made of glass in order to avoid electrical interactions with the discharge. The Pitot tube consisted of a flat-ended cylinder with an external diameter of $D = 6\,\mathrm{mm}$ and an internal diameter of $d = 4\,\mathrm{mm}$. In view of these dimensions and the free-stream flow conditions (see Tab. 1), it was not necessary to apply viscous or rarefaction corrections to the pressure measurements performed with the Pitot probe (Menier, 2007). Although the outer diameter of the Pitot probe is of the same order of magnitude as the pressure gradients above the flat plate, many studies related to high speed rarefied flows showed that it was possible to capture these phenomena if the spatial resolution of the measurement was sufficiently fine (for instance, see Allègre and Bisch (1968)). In this study the minimal value of the vertical displacement step was 1 mm. By moving the Pitot probe of less than one diameter between each measurement point, accurate pressure profiles were obtained by doing a moving average. The validity of this method was verified by Menier et al (2006) on a similar experimental setup. In addition, because of the relatively large size of the Pitot tube compared to the flow phenomena, all measurements refer to the Pitot tube axis location.

2.3.2 Image of the discharge

The flow around the flat plate was visualized with a PI-MAX Gen-II ICCD camera (1024×1024-pixel array) equipped with a VUV objective lens (94 mm, $f/4.1$). The light was collected through a quartz window located in the wall of the test section chamber (see Menier et al (2007) for further details on the optical arrangement). Due to the rarefaction level of the flow, the natural flow field around the plate was experimentally visualized through the glow-discharge flow visualization technique. A description of this visualization method can be found in Fisher and Bharathan (1973). This technique allows shock waves to be visualized in low density flows, where other techniques (for instance, Schlieren) cannot be applied because of the rarefied flow regime. The glow-discharge flow visualization technique consists in using an electric discharge to ionize the air flowing around a model in the test chamber. In this study, a plane-to-plane dc discharge was created by applying a high voltage between two parallel rectangular copper plates separated by a gap of about 300 mm. The flat plate was placed between these large electrodes, leading to a stream of ionized air around the model. The consecutive diffuse light emission is focused on the ICCD camera. Due to air density variations in the shock wave, a change in the light intensity in the resulting picture allows the shock wave to be detected (see Sect. 5). This technique was applied to analyze the flow field in both the natural case (without actuation) and with the heating element. When the plasma actuator was used, this technique was not employed because the bright visible emission of the discharge itself allows visualization of the flow around the flat plate and the shock wave.

2.3.3 Surface temperature measurement

An infrared thermography device was used to measure the surface temperature of the flat plate during experiments when the plasma actuator or the heater was used. Thermal imaging consists of measuring the radiation flux that originates from a surface to determine its temperature. In this study, the thermal images were obtained with a FLIR ThermaCAM SC3000 camera. The spectral range of the IR camera lied between 8 μm and 9 μm. The IR camera was placed on top of the wind tunnel and focused the entire surface of the flat plate through a fluorine window (CaF_2), compatible with the IR wavelength range of the camera. The viewing angle remained unchanged during all the experiments. The camera is equipped with a QWIP-type IR photo-detector composed of a 320×240-pixel array, cooled down at 70 K by a Stirling cryocooler. The aperture of the lens used in this study was $10^\circ \times 7.5^\circ$ (FOV) with an image resolution of 0.55 mrad (IFOV). The focus length between the flat plate surface and the IR camera was $1395\,\mathrm{mm} \pm 10\,\mathrm{mm}$, giving a spatial resolution of $0.77\,\mathrm{mm{\cdot}pixel^{-1}} \pm 0.01\,\mathrm{mm{\cdot}pixel^{-1}}$ along both X and Y axis. Focus of the IR camera was performed before each run of the wind tunnel by placing a heated coin (head side) on the flat plate surface. The IR camera was focused until distinguish the head side of the coin the most clearly as possible. The spatial parameters of images recorded with the IR camera are detailed in Tab. 2. In this study, the images were recorded at a frame rate of 1 Hz, with a digitizing resolution (intensity level) of 14-bit.

Two temperature ranges were used during the measurements, depending on the maximum temperature reached at the actuator surface. The first temperature range lies between 283 K and 453 K, with an accuracy of $\pm 1\%$ or $\pm 1\,^\circ\mathrm{C}$. The second one lies between 323 K and 823 K, with an accuracy of $\pm 2\%$ or $\pm 2\,^\circ\mathrm{C}$. The thermal sensitivity (NEDT), which is the smallest temperature differences detectable by the IR camera, is less than 40 mK for the first range, and less than 120 mK for the second range. The details of the two temperature ranges used in this study are given in Tab. 3. For some experimental configurations, the second temperature

Table 2 Parameters of images recorded during the surface temperature measurements.

Axis	X	Y	Comments
Array size	320 pixel	240 pixel	
FOV	10°	7.5°	
Focus length d	1395 mm	1395 mm	±10 mm
Total FOV (= $2d\tan(FOV/2)$)	244 mm	183 mm	±0.7 %
IFOV	0.55 mrad	0.55 mrad	
Target spot size (= d $IFOV$)	0.77 mm	0.77 mm	±0.01 mm

Table 3 Temperature ranges used for the temperature measurements.

Range	283 K–453 K	323 K–823 K
Accuracy	±1% or ±1 °C	±2% or ±2 °C
NEDT	40 mK	120 mK
Integration time	1.3 ms	0.2 ms
SNR	125	41
Resolution	14-bit	14-bit

range was used because the surface temperature was higher than 453 K. This implied that the IR camera was not able to detect a surface temperature lower than 323 K.

In this study, the flat plate is considered as an opaque object because the transmission coefficient of fused quartz is ≈ 0 for the wavelength range of the IR camera. In addition, the distance between the flat plate and the camera implied that the atmospheric absorption caused by steam and CO_2 is negligible (Minkina and Dudzik, 2009). The transmission coefficient of atmosphere was therefore considered equal to unity. Then, the relation between the black body temperature detected by the IR camera (T_{cam}) and the effective temperature of the object (T_{obj}) can be written as (Minkina and Dudzik, 2009)

$$T_{cam}^4 = \varepsilon_w T_{obj}^4 + (1-\varepsilon_w)\, T_{amb}^4, \tag{2}$$

where ε_w is the emissivity of the object and T_{amb} is the ambient temperature. In this study, T_1 is considered as the ambient temperature. Finally, the surface temperature turns to be

$$T_{obj} = \sqrt[4]{\frac{T_{cam}^4 - (1-\varepsilon_w)\, T_1^4}{\varepsilon_w}}. \tag{3}$$

To estimate the effective temperature T_{obj} of the object surface with Eq. (3), the surface emissivity ε_w needs to be known. In this study, both types of actuator are made with bare aluminum foil, which is a surface having a low emissivity ($\varepsilon_w < 0.1$, the exact value depends on the type of surface). If the object has a low emissivity, the measurement

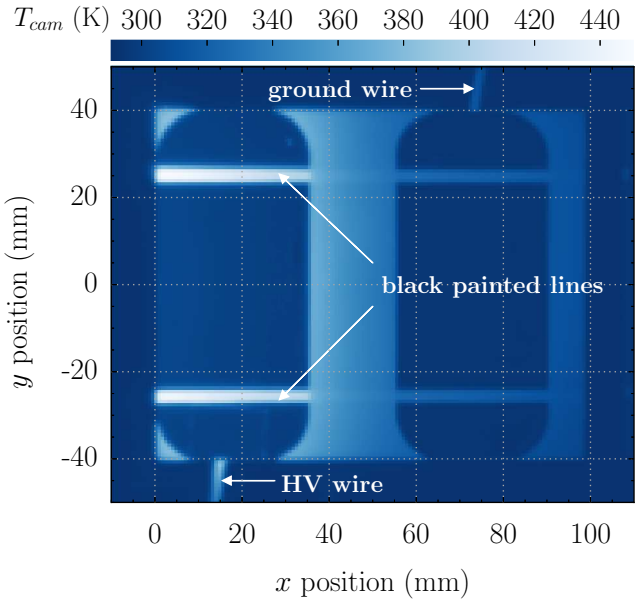

Fig. 4 Thermogram of T_{cam} recorded by the IR camera in the case of the plasma actuator. The longitudinal profiles of the surface temperature are extracted from the two black painted lines (at $y = \pm 25$ mm). The dark rounded rectangles on the flat plate surface are the electrodes. The air ($M_1 = 2$) is flowing from the left to the right.

of its surface temperature is difficult to perform by a radiative measurement method. In a such case, the main contribution in the total amount of thermal radiation detected by the IR camera corresponds to the radiation emitted by the surrounding ambient that is reflected by the object surface (i.e., the term $(1-\varepsilon_w)\, T_{amb}^4$ in Eq. (2)). The radiation emitted by the object itself accounts only for less than 10% (if $\varepsilon_w < 0.1$ and $T_{obj} \sim T_{\mathrm{amb}}$), meaning that a surface having a low emissivity tends to behave as a mirror, in the sense of thermal radiation. Therefore, a surface with an high value for ε_w should be preferred to measure the surface temperature more accurately.

In this study, because electrodes were made with aluminum foil, which have a low value of ε, two longitudinal (i.e., along the X-direction) thin black lines were painted on the flat plate surface (including the electrodes) to assess the surface temperature with the IR camera (see Fig. 4). A high temperature flat black paint was used because such coating has emissivity in the range 0.8–0.95 (Minkina and Dudzik, 2009), making the measurement of the surface temperature less perturbed by the reflected radiation of the surrounding ambient. The black paint was applied over the whole length of the flat plate, meaning the naked surface of the model (i.e., the fused quartz) was covered by the paint. Therefore, the emissivity of fused quartz was not necessary to calculate the surface temperature between the two electrodes. Figure 4 shows a typical thermogram of the temperature T_{cam} detected by the IR camera. The two black painted lines were

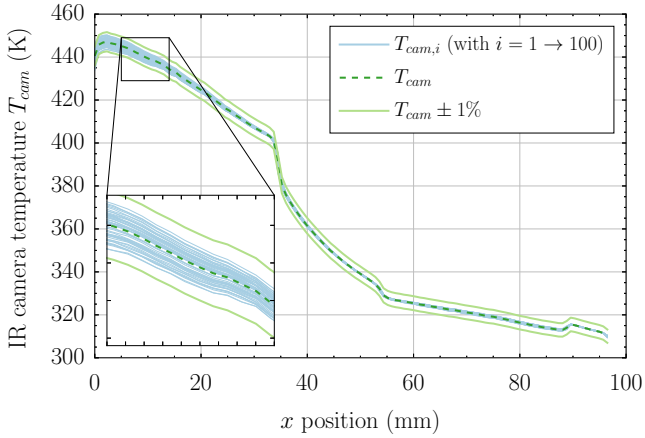

Fig. 5 Typical longitudinal profile of temperature detected by the IR camera in the case of the plasma actuator. The free stream Mach number is 2.

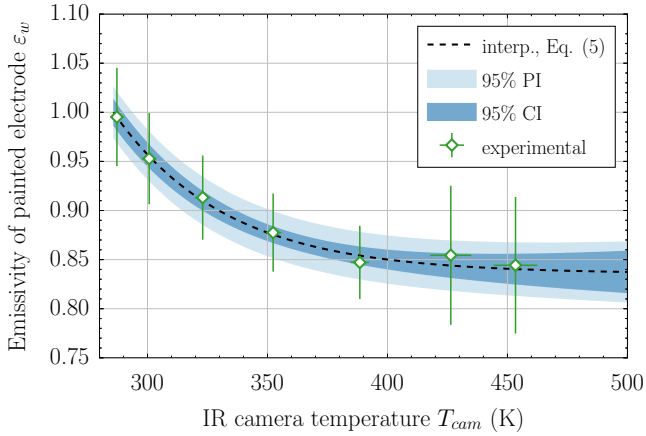

Fig. 6 Emissivity of painted electrode ε_w versus the temperature T_{cam} detected by the IR camera. The free stream Mach number is 2.

located at $y = \pm 25$ mm, and had a length of 100 mm and a width of 4 mm.

For each experimental case, the temperature measurements were performed after waiting until thermal equilibrium had been reached ($\approx$ 15–20 min, Léger et al (2009)). The surface temperature along the flat plate was obtained by post-processing 100 images recorded at 1 Hz with the IR camera. The number of images was chosen as a result of a convergence study. The typical testing time of a single run was approximately 1300 s, including a waiting time for the thermal equilibrium of 1200 s and a measurement duration with the IR camera of 100 s. For the i–th thermogram, two instantaneous longitudinal profiles of surface temperature, $T_{cam,L}(x)$ and $T_{cam,R}(x)$, are extracted from the IR image. These two profiles corresponded to the temperature distribution of the black painted lines at $y = \pm 25$ mm and were averaged over the width of the painted lines (i.e., over 5 pixels in the y-direction). Then, the longitudinal temperature profile of the i–th thermogram $T_{cam,i}(x)$ was obtained by averaging $T_{cam,L}(x)$ with $T_{cam,R}(x)$. Finally, the longitudinal temperature profile $T_{cam}(x)$ of a given experimental case was obtained by averaging the instantaneous profiles.

Figure 5 shows a typical longitudinal profile of T_{cam} obtained from the instantaneous profiles $T_{cam,i}$. Description of the profile shape is given in Sect. 4.1. The instantaneous profiles are weakly scattered around the average value, within a range of less than 1% of T_{cam}. This scattering of experimental data during the measurement was taken into account as a source of random uncertainty in the evaluation of the total uncertainty of the surface temperature (see Sect. 2.3.4). The homogeneity of the temperature distribution along the model span (i.e., along the Y-axis) was evaluated by performing tests with a plasma actuator having a black line painted along its span (at $x = 17.5$ mm). These measurements showed that the temperature was homogeneous over more than 80% of the model span. The order of magnitude of the temperature fluctuations along the span is few percents of the average temperature (Joussot et al, 2010). In this study, the spanwise fluctuations of the temperature were estimated at $\pm 3\%$. Therefore, the surface temperature $T_{cam}(x)$ estimated from the local measurements at the two positions $y = \pm 25$ mm was representative of the overall surface temperature along the span. The slight fluctuations of the temperature along the span of the model was taken into account in considering a fixed uncertainty of $\Delta T_{cam}^{sym} = \pm 3\%$ in the estimation of the total uncertainty of the surface temperature (see Sect. 2.3.4). In addition, repeatability tests were performed for both the plasma actuator and the heater. For a given set of electrical parameters (voltage and current), the values of surface temperature $T_{cam}(x)$ recorded for several single runs (with the actuator switched-off between each run) were similar at $\pm 1\%$. The repeatability of the temperature measurements was taken into account in considering a fixed uncertainty of $\Delta T_{cam}^{rep} = \pm 1\%$ in the total uncertainty of the surface temperature (see Sect. 2.3.4).

The emissivity of the flat plate surface was measured using the direct emissivity measurement method. This consisted in measuring locally the surface temperature of the black painted area simultaneously with both the IR camera (T_{cam}) and a K-type thermocouple (T_{thc}, with an accuracy of $\pm 1.5\,^{\circ}$C) flush mounted on the flat plate surface (at $x = 20$ mm and $y = -25$ mm). From Eq. (3), emissivity of the painted electrode ε_w turns to be

$$\varepsilon_w = \frac{T_{cam}^4 - T_1^4}{T_{thc}^4 - T_1^4}. \tag{4}$$

Figure 6 shows the variation in ε_w as a function of the surface temperature T_{cam} recorded by the IR camera. The 95% confidence (95% CI) and prediction (95% PI) intervals (see Sect. 2.3.4) are also reported in Fig. 6. The error-bars

represent the total uncertainty $\Delta\varepsilon_w$ (see Sect. 2.3.4). The average value of $\Delta\varepsilon_w$ was estimated at $\pm 4.6\%$ over the temperature range 283 K–453 K of the IR camera, and $\pm 7.9\%$ over the second range (323 K–823 K). The variation of the painted electrode emissivity according to the temperature detected by the IR camera can be approached by

$$\varepsilon_w = 1 - a\left[1 - exp\left(\frac{T_{cam,off} - T_{cam}}{b}\right)\right], \tag{5}$$

where $a = 0.164 \pm 0.008$ and $b = 46.8\,\mathrm{K} \pm 6.7\,\mathrm{K}$ are the best-fit parameters with their corresponding standard errors (see Sect. 2.3.4) obtained by fitting (least-squares method) the experimental data to a given model, and $T_{cam,off} = 285.8\,\mathrm{K} \pm 1.9\,\mathrm{K}$ is the initial temperature, corresponding to the temperature of the case without surface heating. In this study, the emissivity coefficient is expressed as a function of T_{cam} to minimize the error committed if ε_w was kept constant. If the flat plate is considered as a black body (i.e., $\varepsilon_w = 1$), the effective temperature of the flat plate will be underestimated by 4.5%. For a given value of T_{cam} measured by the IR camera, the effective temperature of the electrode surface T_w was calculated with Eqs. (3) and (5). Repeatability tests were performed with the plasma actuator to check that emissivity of the black painted lines remained unchanged after several tests with the discharge.

The total uncertainty ΔT_w of the effective surface temperature of the flat plate (see Sect. 2.3.4) takes into account the different sources of uncertainties (accuracy, spanwise fluctuations, repeatability, standard deviation) of the different variables (T_{cam}, T_1, ε_w) used to calculate T_w. The average value of ΔT_w was estimated at $\pm 5.2\%$ over the temperature range 283 K–453 K of the IR camera, and $\pm 6.3\%$ over the second range (323 K–823 K).

2.3.4 Measurement uncertainty and confidence intervals

The measurement uncertainties are estimated according to Abernethy et al (1985) and the error propagation law suggested by Kline and McClintock (1953). The total uncertainty ΔR of an experimental result R, which is a function of several variables, takes into account the systematic uncertainties and the random uncertainties of the different variables. In this study, the systematic uncertainty includes calibration, accuracy, spatial homogeneity, and repeatability of the experimental measurements. The random uncertainty corresponds to the standard deviation of the experimental measurements. According to Kline and McClintock (1953); Abernethy et al (1985), the total uncertainty ΔT_w of the surface temperature $T_w = f\left(T_{cam}, T_1, \varepsilon_w\right)$ is expressed as follows

$$\Delta T_w = \left[\left(\frac{\partial f}{\partial T_{cam}}\right)^2 \left(\Delta T_{cam}^{acc} + \Delta T_{cam}^{sym} + \Delta T_{cam}^{rep}\right)^2 + \left(\frac{\partial f}{\partial T_1}\Delta T_1^{acc}\right)^2 + \left(\frac{\partial f}{\partial \varepsilon_w}\Delta\varepsilon_w\right)^2 + \left(\frac{t_{95}}{\sqrt{N}}\frac{\partial f}{\partial T_{cam}}T_{cam}^{std}\right)^2\right]^{1/2}, \tag{6}$$

where ΔT_{cam}^{acc} and ΔT_1^{acc} correspond to the uncertainty in accuracy of temperature measurements, ΔT_{cam}^{sym} corresponds to the uncertainty due to the spanwise variation of the temperature, ΔT_{cam}^{rep} corresponds to the uncertainty due to the repeatability of temperature measurements, $\Delta\varepsilon_w$ is the total uncertainty of the surface emissivity, t_{95} is the quantile of a two-tailed Students t-distribution with a confidence interval of 95%, N is the number of samples used to calculate T_{cam} (i.e., the number of IR images), and T_{cam}^{std} is the standard deviation of T_{cam}.

The total uncertainties Δp_0, Δp_1, and Δp_{Pitot} of the stagnation pressure p_0, the static pressure p_1, and the Pitot pressure p_{Pitot}, respectively, are expressed as follows

$$\Delta p_{0/1/Pitot} = \left[\left(\Delta p_{0/1/Pitot}^{acc} + \Delta p_{0/1/Pitot}^{lin}\right)^2 + \left(\frac{t_{95}}{\sqrt{N}}p_{0/1/Pitot}^{std}\right)^2\right]^{1/2}, \tag{7}$$

where $\Delta p_{0/1/Pitot}^{acc}$ is the accuracy uncertainty, $\Delta p_{0/1/Pitot}^{lin}$ corresponds to the linearity uncertainty of the pressure gauge calibration, and $p_{0/1/Pitot}^{std}$ is the standard deviation of the pressure measurements. The average value of $\Delta p_{0/1/Pitot}$ was typically within $\pm 2\%$.

The total uncertainty of the shock wave angle is discussed in Sect. 5.

The confidence (CI) and prediction (PI) intervals with $1 - \alpha/2$ confidence were obtained with the following relations, respectively

$$\hat{y}_i \pm t_{1-\alpha/2,\upsilon}\left\{s^2\left[\frac{1}{n} + \frac{(x_i - \bar{x})^2}{\sum_{j=1}^{n}(x_j - \bar{x})^2}\right]\right\}^{1/2}, \tag{8}$$

$$\hat{y}_i \pm t_{1-\alpha/2,\upsilon}\left\{s^2\left[\frac{1}{n} + \frac{(x_i - \bar{x})^2}{\sum_{j=1}^{n}(x_j - \bar{x})^2} + 1\right]\right\}^{1/2}, \tag{9}$$

where $\hat{y}_i$ is the predicted value, $t_{1-\alpha/2,\upsilon}$ is the quantile of Student's t-distribution (two-tailed), $1 - \alpha/2$ is the confidence, υ is the degrees of freedom, s is the standard deviation of the residual error, n is the number of samples, x_i is the value for which $\hat{y}_i$ is calculated, x_j is the jth experimental

value, and $\bar{x}$ is the mean value of the experimental data. The standard errors of best-fit parameters were calculated with the Python-based Kapteyn package (Terlouw and Vogelaar, 2012) by taking into account errors both in x and y using the effective variance method (i.e., weighted fits). The 2D plots were produced in Python, using the NumPy and Matplotlib environment (Hunter, 2007; Oliphant, 2007).

3 Numerical approach

In the present work, the numerical simulations were performed by using the 2D compressible Navier-Stokes equations with the boundary conditions adapted to match the physical phenomena involved in the slip-flow flow regime.

3.1 Governing equations

The 2D full compressible Navier-Stokes equations are used in the conservative form to describe the air flow around the flat plate. These equations are:

– the continuity equation :

$$\frac{\partial \rho}{\partial t} + \frac{\partial \rho u_i}{\partial x_i} = 0, \tag{10}$$

where x_i is the space coordinate, t is the time, ρ is the density, and u_i is the velocity in the space direction x_i.

– the momentum conservation equation :

$$\frac{\partial \rho u_j}{\partial t} + \frac{\partial \left(\rho u_j u_i + p\delta_{ij} - \tau_{ij}\right)}{\partial x_i} = 0, \tag{11}$$

where p is the pressure, τ_{ij} is the viscous shear stress tensor, and δ_{ij} is Kronecker's symbol. We assume that the fluid is Newtonian, so the viscous shear stress tensor can be written as:

$$\tau_{ij} = \mu\left(\frac{\partial u_i}{\partial x_j} + \frac{\partial u_j}{\partial x_i}\right) - \delta_{ij}\frac{2}{3}\mu\frac{\partial u_k}{\partial x_k}, \tag{12}$$

where μ is the viscosity coefficient.

– the energy conservation equation:

$$\frac{\partial \rho e_t}{\partial t} + \frac{\partial \left(\rho u_i e_t + u_i p - u_i \tau_{ij} + q_i\right)}{\partial x_i} = 0, \tag{13}$$

where $e_t = e + \left(\rho \Sigma u_i^2\right)/2$ is the total energy, e is the internal energy, and q_i is the heat flux in the space direction i. The Prandtl number is 0.7, corresponding to air gas.

3.2 Boundary conditions

Because of the rarefied regime, the boundary conditions applied in the equation system (10)–(13) are the slip velocity u_s and the temperature jump T_j conditions on the solid wall ($z = 0$). The complete wall boundary condition proposed by Kogan (1969) is used, taking into consideration the first-order Knudsen number conditions. The slip velocity and the temperature jump at the wall are expressed, respectively, by

$$u_s(x) = 1.012\frac{\mu_w}{\rho_w(x)}\left[\frac{2m}{k_B T_w(x)}\right]^{1/2}\left(\frac{\partial u_x(x)}{\partial z}\right)_{z=0}, \tag{14}$$

$$\begin{aligned} T_j(x) =& T_w(x) + \frac{2 - a\,\alpha_e}{\alpha_e}\left[\frac{2m}{k_B T_w(x)}\right]^{1/2} \times \\ & \frac{\lambda_{T_w}(x)\,m}{k_B \rho_w(x)}\left(\frac{\partial T(x)}{\partial z}\right)_{z=0}, \end{aligned} \tag{15}$$

where μ_w and λ_{T_w} are the viscosity and the thermal conductivity, respectively, evaluated at the wall temperature T_w, ρ_w is the density, k_B is the Boltzmann constant, m is the mass, u_x is the tangential velocity to the wall, α_e is the coefficient of energy accommodation at the wall, and a is a numerical coefficient defined by Kogan (1969). In this study, a full accommodation assumption is considered (i.e., $\alpha_e = 1$).

In the present work, although several types of effects are involved when the plasma actuator is used (for instance, bulk heating, thermal disequilibrium, and ionization), only the heating of the flat plate surface was considered for the numerical simulations. Neither the plasma nor the electric field were simulated here. The surface heating of the flat plate was simulated by fixing different temperature distributions for the Dirichlet boundary condition on the model wall. To reproduce numerically the surface heating measured experimentally when the discharge was fired, the temperature distributions (i.e., $T_w = f(x)$) obtained from the temperature measurements by the IR camera (see Sect. 4.1) were used as boundary condition for the upper surface of the model.

In this study, the surface temperature evolved with the longitudinal position x, which was not the case in a previous study of our group (Parisse et al, 2009), where the surface temperature was kept constant along the flat plate surface. For the rest of the flat plate and the whole domain, an initial temperature of 163 K was set. At the upper and lower boundaries of the physical domain simulated, a zero gradient condition was imposed. The same type of condition was used for the boundary downstream the model. An inflow condition was set for the boundary upstream the model.

3.3 Numerical scheme

The numerical code uses a structured grid divided into 3 blocks for parallel computing purposes, with a total num-

ber of 108 096 cells. The minimum space step (0.5 mm), was chosen as a result of the convergence study and also taking into account the mean free path value in the free stream (see Tab. 1). The unsteady compressible Navier-Stokes equations are discretized according to an explicit cell-centered finite volume method. The convective block (Euler) is discretized using a WENO 3rd-order accurate TVD-upwind, cell-centered finite volume scheme. The associated Riemann solver is HLLC (Harten-Lax-van Leer-Contact). The diffusive block is then discretized with a centered finite difference scheme. Temporal integration is performed by a 2nd-order Runge-Kutta procedure. The CFL coefficient used to carry out the simulations was 0.75.

This code has been validated on numerous test cases, especially for supersonic and hypersonic rarefied flows (Markelov et al, 2000). In the present work, the numerical code does not use several species, and only the macroscopic temperature is considered to describe the flow. Neither the rotational temperature nor the vibrational one are used, meaning the flow is considered at thermal equilibrium.

4 Characterization of actuators

4.1 Plasma actuator

The discharge was created by applying a negative dc potential to the active electrode. Figure 7 shows the current-voltage characteristic (I_{HV}–V_{HV}) of the plasma actuator. The discharge ignites at around $V_{ign} = -0.36\,\mathrm{kV} \pm 0.01\,\mathrm{kV}$, and can be sustained down to around $V_s \approx -2.5\,\mathrm{kV}$. Within this range the discharge current increases with the applied voltage as

$$I_{HV} = a\,(V_{ign} - V_{HV})^n\,, \tag{16}$$

where $a = 69.2\,\mathrm{mA{\cdot}kV^{-n}} \pm 0.9\,\mathrm{mA{\cdot}kV^{-n}}$ and $n = 1.28 \pm 0.03$ are the best-fit parameters with their corresponding standard errors. V_{ign} is the ignition voltage in kV. This behavior corresponds to the abnormal glow discharge regime (Raizer, 1991).

Previous works (Menier et al, 2007; Léger et al, 2009; Parisse et al, 2009) have shown that for this geometry one of the effects of the plasma actuator on the flow field is caused by the heating of the surface. The main contribution to the cathode heating is the bombardment of energetic neutrals and returning ions, in particular positive ions (Raizer, 1991). Because the motion of ions is directed by the electric field and not by the flow field, they can directly bombard the cathode. Their impact energy is converted to heat into the cathode (the surface heating) and extraction of electrons at the cathode surface (secondary emission). This takes place in the dark area above the cathode (the Faraday's dark space,

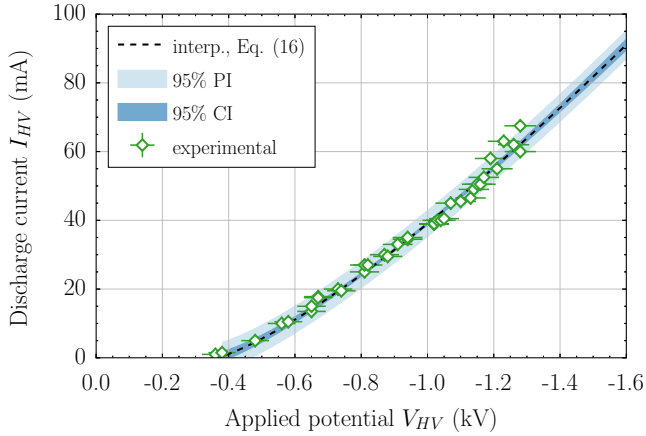

Fig. 7 Current-voltage characteristic of the plasma actuator in a Mach 2 air flow.

see Sect. 6.1), which is the discharge region where the electric field is the strongest. Neutrals are not directed by the electric field but they can bombard the cathode trough successive elastic collisions with charged particles. Since the degree of ionization in a glow discharge plasma is rather low, the most abundant species bombarding the cathode are neutrals (Raizer, 1991). Because the flat plate is beveled, the electric field is stronger in the vicinity of the leading edge (Léger et al, 2009). The non-uniform distribution of the electric field above the cathode induces an intensification of ions bombardment, and thus an increase in the surface temperature of the cathode in this region. The longitudinal distribution of the surface temperature is therefore not constant along the flat plate, as evidenced by the temperature measurements performed with the IR camera (see Fig. 8).

The longitudinal distribution of the surface temperature measured for several discharge currents with the IR camera is presented in Fig. 8a. The highest surface temperatures are measured close to the leading edge. Downstream the active electrode, the flat plate is heated due to the thermal conduction inside the flat plate. The lowest temperatures are measured at the trailing edge of the flat plate. The decreasing shape of the longitudinal temperature distribution is not caused by the interaction between the air flow and the discharge. For a given value of I_{HV}, the plasma discharge induces a similar heating of the flat plate without the Mach 2 flow and with a static pressure set to 8 Pa (not shown here). In this case, the temperature distribution is similar both in terms of value and shape. This result confirms that the heating of the flat plate surface results from the presence of the plasma discharge. The thermal equilibrium of the cathode temperature is reached after 15–20 min, meaning that the magnitude order of the time scale of surface heating is few tens of minutes. Over the range of electrical configurations tested with the plasma actuator, the maximum surface tem-

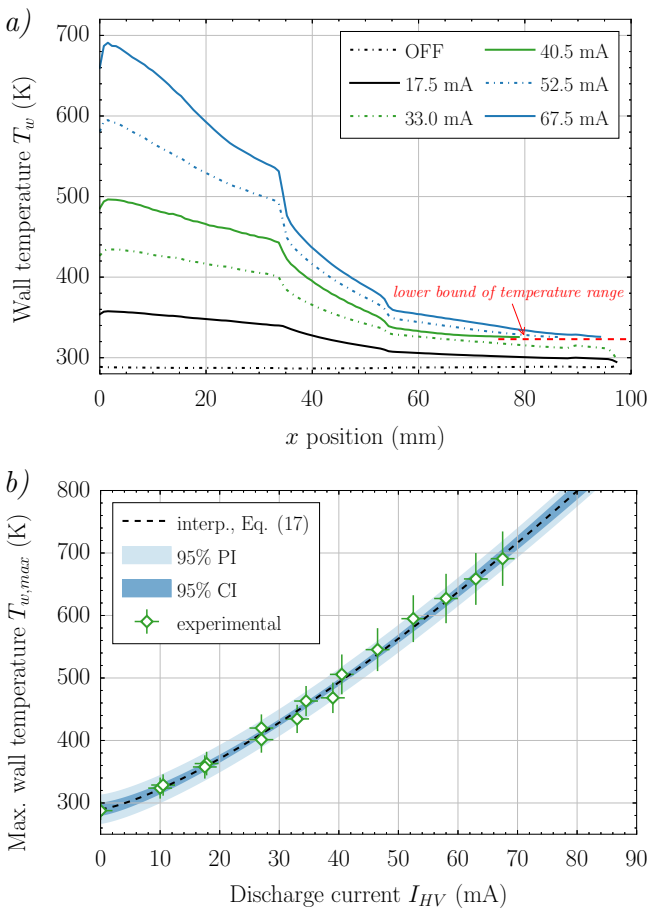

Fig. 8 Surface temperature in the case of the plasma actuator: *(a)* longitudinal distribution of the wall temperature T_w along the flat plate, and *(b)* variation of the maximum wall temperature $T_{w,max}$ as a function of the discharge current I_{HV}. The free stream Mach number is 2.

perature $T_{w,max}$ appears to evolve with the discharge current (see Fig. 8b) as

$$T_{w,max} = a\,(I_{HV})^n + T_{w,off}, \tag{17}$$

where $a = 1.52\,\mathrm{K{\cdot}mA^{-n}} \pm 0.33\,\mathrm{K{\cdot}mA^{-n}}$ and $n = 1.33 \pm 0.05$ are the best-fit parameters with their corresponding standard errors, and $T_{w,off} = 290.0\,\mathrm{K} \pm 4.3\,\mathrm{K}$ is the wall temperature in the case of the natural flow.

4.2 Heating element

The surface heating of the flat plate induced by the plasma actuator was experimentally reproduced by using the non uniform heater described previously (see Sect. 2.2). The flat plate surface was heated by applying a dc potential to the heater. Figure 9 shows the current-voltage characteristic (I_{HE}–V_{HE}) of the heater. Because the heater is a resistive device, the current is linear with the applied voltage (slope of $1/R_{HE}$, $R_{HE} = 16.81\,\Omega \pm 0.03\,\Omega$ is the resistance value of the heater).

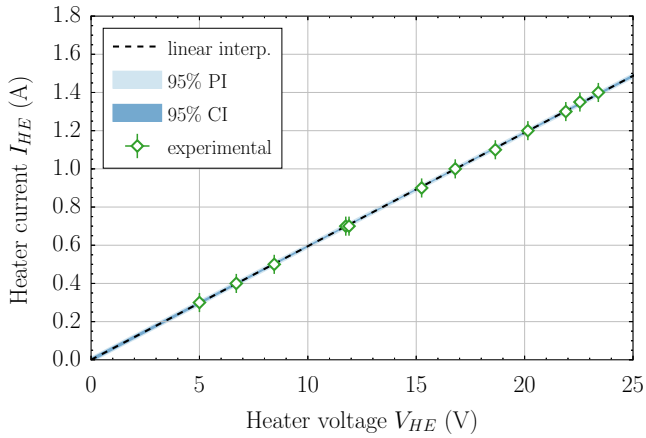

Fig. 9 Current-voltage characteristic of the heater in a Mach 2 air flow.

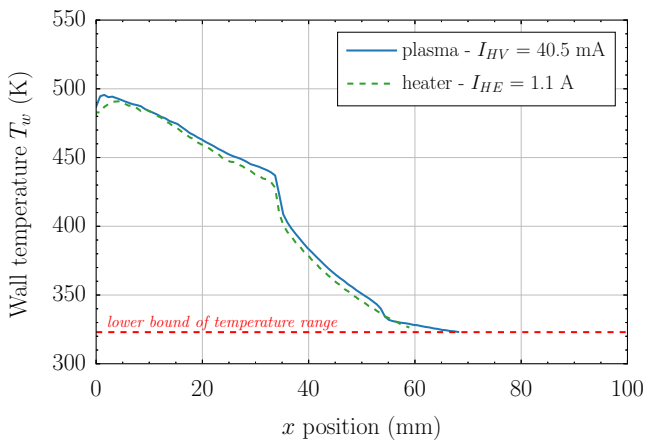

Fig. 10 Comparison of wall temperature distribution along the flat plate between the plasma actuator at $I_{HV} = 40.5\,\mathrm{mA}$ and the heater at $I_{HE} = 1.1\,\mathrm{A}$. The free stream Mach number is 2.

The spatial distribution of the wall temperature measured with the plasma actuator is reproduced by using the heater with a non-uniform distribution of the resistive wire. Several wire distributions were tested to obtain a temperature distribution similar to the one measured with the plasma actuator. With this particular wire distribution for the heater, a similar value of $T_{w,max}$ than that measured with the plasma actuator (for a given value of I_{HV}) can be achieved by supplying the heater with an adequate value for the current I_{HE} (see Fig. 10). Therefore, the temperature distribution $T_w(x)$ and the maximal surface temperature $T_{w,max}$ can be reproduced with the heater, by optimizing the wire distribution and the heater current, respectively. A maximum wall temperature up to $T_{w,max} \approx 550\,\mathrm{K}$ can be reached with the heater (see Fig. 11). Higher values of $T_{w,max}$ are not allowed due to the physical characteristics of the polyimide film (working temperature below 553 K). However, a large part of the values of $T_{w,max}$ measured with the plasma actuator can be investigated with the heater. Over the range of electrical configura-

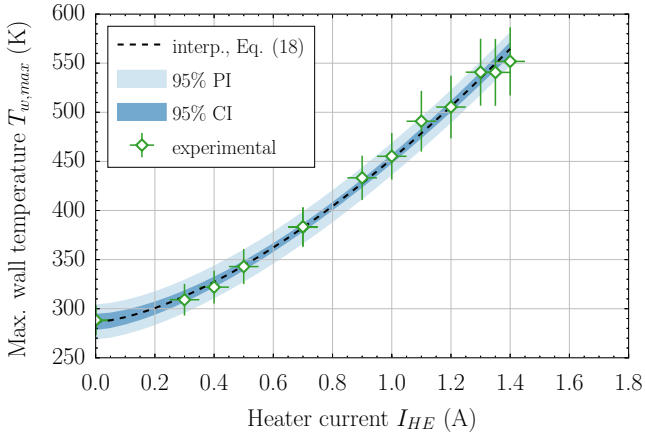

Fig. 11 Maximum wall temperature $T_{w,max}$ according to the heater current I_{HE}. The free stream Mach number is 2.

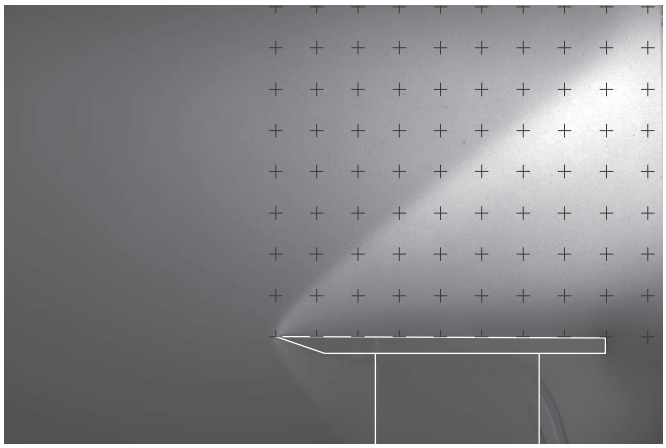

Fig. 12 Image of the natural flow field around the flat plate obtained with the glow-discharge flow visualization technique (300 ICCD images averaged and post-processed, individual exposure time of 50 ms). The free stream Mach number is 2.

tions tested with the heating element, the maximum surface temperature $T_{w,max}$ of the heater evolves with the current I_{HE} as

$$T_{w,max} = a\,(I_{HE})^n + T_{w,off}, \tag{18}$$

where $a = 166.0\,\mathrm{K{\cdot}A^{-n}} \pm 3.4\,\mathrm{K{\cdot}A^{-n}}$ and $n = 1.53 \pm 0.05$ are the best-fit parameters with their corresponding standard errors, and $T_{w,off} = 286.5\,\mathrm{K} \pm 2.2\,\mathrm{K}$ is the wall temperature of the heater in the case of the natural flow.

5 The baseline flow

The flow field around the flat plate was first investigated without any actuation, corresponding to the study of the natural flow (namely, the baseline). In this case, the shock wave was experimentally visualized with the glow-discharge flow visualization technique (see Sect. 2.3.2). Figure 12 shows an image of the baseline around the flat plate visualized with the ICCD camera. This image results from the averaging and post-processing of 300 snapshots of the flow field recorded with the ICCD camera. The contrast was enhanced with ImageJ software (Schneider et al, 2012) in order to distinguish the shock wave position more precisely than is possible from a single raw image. The air flows from the left to the right.

The shock wave is readily recognized on the image captured with the ICCD camera, enabling the estimation of its shape. In our conditions, the shock wave shape for the baseline is hyperbolic and can be described by

$$x = c_1 + c_2 \left[1 + \left(\frac{z}{c_3} \right)^2 \right]^{1/2}, \tag{19}$$

where x and z are the shock wave coordinates in the Cartesian coordinate system (centered on the leading edge), and c_1, c_2 and c_3 are the geometric coefficients of the hyperbola. This type of shock wave shape is consistent with shapes reported in the literature. The shock wave angle β corresponds to the angle of the hyperbola asymptote (i.e., the Mach angle). The coefficients c_1, c_2 and c_3 are estimated by fitting (least squares method) the shock wave position on the ICCD images, enabling the shock wave angle to be calculated. For the baseline, the value of the shock wave angle is $\beta_{off} = 36.71^\circ \pm 0.68^\circ$. The error corresponds to the total uncertainty $\Delta\beta$ calculated according to Abernethy et al (1985). For a given experimental configuration, the value of β results in the repeated analysis (three times) of the same series of images. The total uncertainty $\Delta\beta$ is therefore estimated by $(t_{95}/\sqrt{N})\beta_{std}$, where $N = 3$ is the number of pass, $t_{95} = 3.1824$ is the corresponding value of the quantile of a two-tailed Students t-distribution with a confidence interval of 95%, and β_{std} is the standard deviation of β. The shock wave is slightly detached from the leading edge of the plate because of the rarefaction effects. The magnitude order of the shock wave stand-off distance is 1–2 mm. For the baseline, the longitudinal distribution of the surface temperature measured with the IR camera along the flat plate is homogeneous: T_w ranges between 286.7 K and 288.8 K with an average value of ≈ 287.4 K (see Fig. 8a, black dash-dot line).

The baseline of the Mach 2 flow field was simulated with the WENO code described in Sect. 3. The simulation was run with the input parameters corresponding to the experimental flow conditions (see Tab. 1). The resulting Mach number field is shown in Fig. 13. The global shape of the shock wave is well reproduced as well as the stand-off of the shock wave ahead of the leading edge. The longitudinal distribution of the surface temperature is homogeneous with an average value over the flat plate of 282.8 K. The underestimation of the surface temperature for the simulated baseline can be due to the wall conditions (slip velocity and

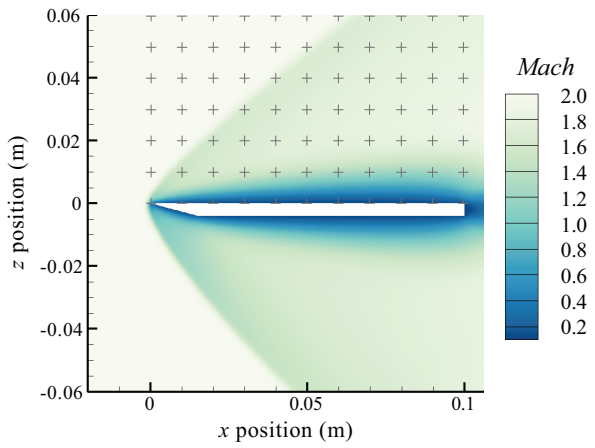

Fig. 13 Mach number flow field obtained from the WENO simulation of the baseline. The free stream Mach number is 2.

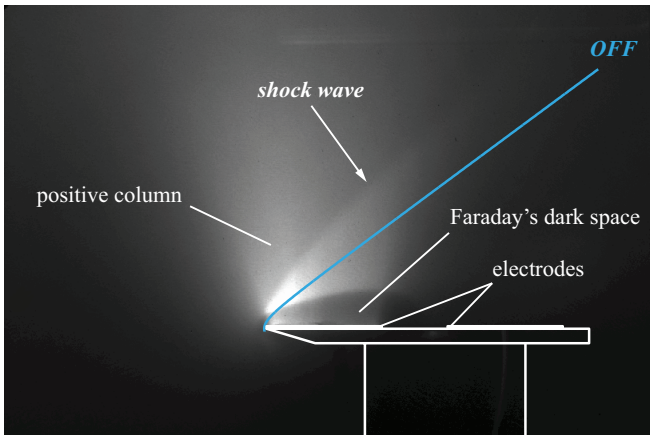

Fig. 14 ICCD image of the flow field modified by the plasma actuator ($V_{HV} = -1.57\,\text{kV}$ and $I_{HV} = 74\,\text{mA}$). The solid line represents the shock wave shape of the baseline. The free stream Mach number is 2.

temperature jump) used to simulate the flow field. The shock wave position is estimated by detecting the wall-normal position of maximum slope of the dynamic pressure field (McCroskey et al, 1966). The fitting of the shock wave shape with Eq. (19) gives a shock wave angle for the simulated baseline of $\beta = 37.39°$, which is slightly larger than the experimental value. This discrepancy is due to a slight overestimation of the shock layer thickness by the numerical code (see Sect. 6.2).

6 Analysis of the shock wave angle increase

6.1 Modifications induced by the plasma actuator

When the high voltage is switched on, gas above the cathode is ionized and a weakly ionized plasma is created. Figure 14 shows an image taken with the ICCD camera of the flat plate with the plasma actuator working. The plasma discharge exhibits a plume-like shape slightly slanted in the upstream direction, and is divided into two main distinct zones. The first one is the Faraday's dark space, corresponding to the dark area around the cathode (Raizer, 1991). Because a shock wave is present, this dark space is slightly slanted in the upstream direction. The Faraday's dark space has a thickness ranged approximately between 5 mm and 15 mm, allowing it to overtake the leading edge of the flat plate. Beyond the Faraday's dark space, there is a large luminous region called the positive column where the ionization process takes place (Raizer, 1991). Into the positive column, the shock wave position corresponds to the oblique gradient of luminosity observed above the flat plate. The plasma discharge induces a modification of the shock wave that is deflected outward from the flat plate surface as illustrated in Fig. 14. The shock wave shape of the baseline (solid line) is superimposed on the image to make the comparison easier. For the electrical configurations experimentally tested, the hyperbolic shape

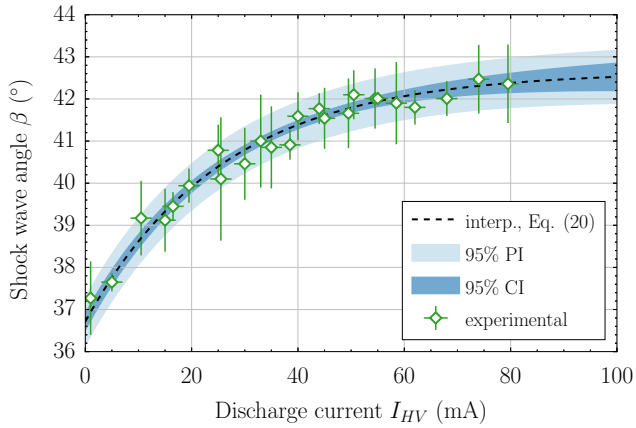

Fig. 15 Shock wave angle β versus the discharge current I_{HV}. The free stream Mach number is 2.

of the shock wave is preserved, allowing Eq. (19) to be used to estimate the shock wave angle. In addition, the magnitude order of the shock wave stand-off distance remains within the 1–2 mm-range.

Figure 15 shows the variation in the shock wave angle with the discharge current. It can be seen that the higher the discharge current is, the greater the increase in the shock wave angle is. This variation can be approached by

$$\beta = a\left[1 - exp\left(\frac{-I_{HV}}{b}\right)\right] + \beta_{off}, \tag{20}$$

where $a = 5.94° \pm 0.21°$ and $b = 25.81\,\text{mA} \pm 3.04\,\text{mA}$ are the best-fit parameters with their corresponding standard errors, and $\beta_{off} = 36.71°$ is the shock wave angle of the experimental baseline (see Sect. 5).

6.2 Analysis of the thermal effects

In the case of the rarefied flow regime, one of the main effects expected to be responsible for modifying the shock wave is heating of the model surface (Semenov et al, 2002; Bletzinger et al, 2005), which induces a displacement effect. The flow viscosity above the heater is modified, leading to an increase in the boundary layer thickness δ_{99}, and, consequently, a shift of the shock wave outward of the flat plate surface (i.e., β increases). In this experiment, a Pitot survey of the flow above the cathode shows the increase in δ_{99} (see Fig. 16a). At the longitudinal position $x = 17.5$ mm (i.e., in the middle of the cathode), the shape of the Pitot profiles indicates that the shock wave and the boundary layer are merged. The boundary layer thickness is therefore estimated by measuring the wall-normal position of the maximum pressure. In the case of the baseline, $\delta_{99} = 11.7$ mm, whereas $\delta_{99} = 18.7$ mm for a plasma discharge with $V_{HV} = -1.47$ kV and $I_{HV} = 39$ mA, showing the displacement effect induced by the plasma actuator.

The longitudinal distribution of the surface temperature measured with the IR camera was implemented into the numerical code as the boundary condition for the upper surface temperature of the flat plate model. In this study, the surface temperature gradient due to the electric field was taken into account, which was not the case in the previous study by our group (Parisse et al, 2009). In order to simulate a Pitot survey of the flow above the flat plate, a synthetic Pitot pressure was calculated from the dynamic pressure and the flow conditions (Menier, 2007). Figure 16b shows the synthetic Pitot profiles above the flat plate at $x = 17.5$ mm, for different cases of a simulated surface heating.

Whatever the case, the profile shape is different from the one measured experimentally. The shape of the experimental Pitot profiles exhibits a single 'knee' at the wall-normal position of the maximum pressure, identified as the edge of the boundary layer and meaning that the boundary layer if fully merged with the shock wave (McCroskey et al, 1966). Nevertheless, the pressure profiles calculated from the numerical simulations for the same x-position present two 'knees'. The first one, located at the wall-normal position of the maximum pressure, corresponds to the lower side of the shock wave. The second knee is observed at a lower z-position and corresponds to the edge of the boundary layer. This shape of the synthetic Pitot profiles obtained from the numerical simulations suggests that the boundary layer and the shock layer are not merged and that a layer of inviscid flow separates them (McCroskey et al, 1966).

To explain the discrepancies between experimental and numerical Pitot profiles, the boundary conditions used in the numerical simulations can be considered. Because this study lies with the slip-flow regime ($Kn \sim 0.001$), the slip velocity and the temperature jump were used at the model

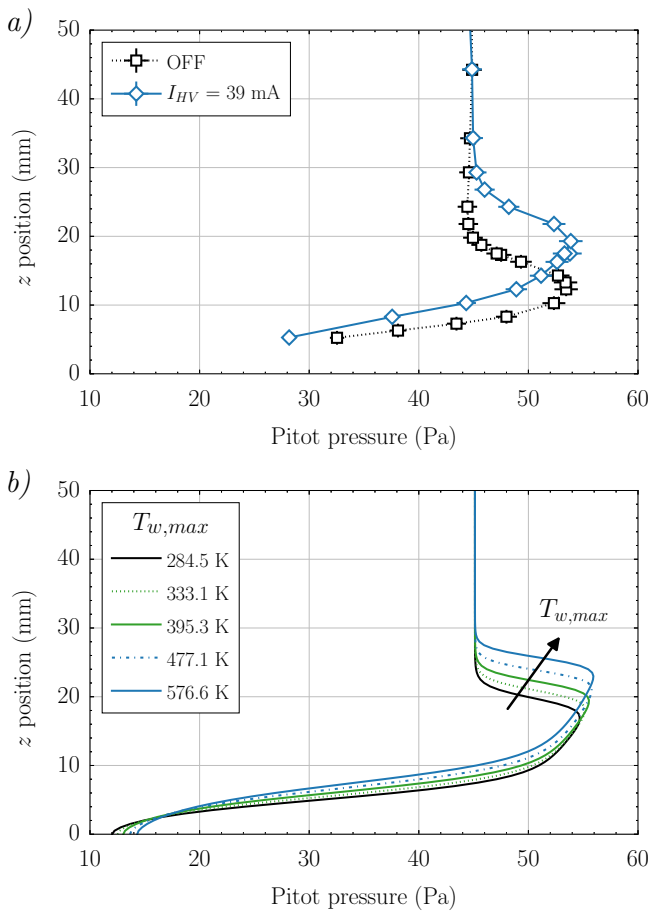

Fig. 16 Pitot pressure profiles in the wall-normal direction at $x = 17.5$ mm in the case of: *(a)* plasma actuator ($V_{HV} = -1.47$ kV and $I_{HV} = 39$ mA and *(b)* numerically simulated surface heating, where the temperature mentioned in the legend is $T_{w,max}$. The free stream Mach number is 2.

wall (see Sect. 3.2). Analysis of Fig. 16 suggests that the downstream limit of the merged layer is reached earlier in the numerical simulations ($x < 17.5$ mm) than in the experiments ($x > 17.5$ mm). This earlier development of the inviscid layer, between the boundary layer and the shock wave, means that in the vicinity of the leading edge, both the slip velocity and the temperature jump could not be well adapted to our experimental conditions. In particular, the high temperature values set close to the leading edge to comply with the temperature measurements may interfere with the temperature jump. Another source of differences could concern the coefficient of energy accommodation at the wall (α_e in Eq. (15)). In this study, it was taken equal to unity. While numerous authors used this assumption ($\alpha_e = 1$) for simplicity reasons, it is known that α_e can depend on the gas composition and the surface material (Springer, 1971). Further numerical simulations will be achieved in order to check if a lower value of α_e could be more representative of the experimental conditions (i.e., an air flow and aluminum elec-

trodes). However, the numerical Pitot profiles in Fig. 16b confirm that the surface heating induces a displacement effect. The boundary layer thickness is increased, shifting outward the shock wave in return. Because an earlier development of the inviscid layer is observed, the shock wave angle β is slightly overestimated in the numerical simulations.

Another possible effect produced by the plasma discharge is bulk heating of the gas above the flat plate surface, inducing an increase in the thermodynamic temperature. The ideal gas equation is used to define the thermodynamic temperature and, even in a non-equilibrium situation of a diluted gas, this equation can be applied to determine the translational temperature T_{tr} of the gas. However, in rarefied flows, the non-equilibrium behavior of the temperature may appear, in the sense of the translational (T_{tr}), rotational (T_{rot}), and vibrational (T_{vib}) temperatures could take different values. Under certain conditions of the rotational-translational relaxation, equilibrium between translational and rotational modes takes place, meaning that T_{rot} can be used to determine T_{tr} (i.e., the gas temperature). To determine if the rotational modes are in equilibrium with the translational ones, one can use the number of gas kinetic collisions (Z_{R-T}) necessary to establish the rotational-translational equilibrium. The value of Z_{R-T} depends on the gas composition and its temperature. Chernyi et al (2002) give the value of Z_{R-T} for nitrogen (N_2) at several gas temperatures. For the present experimental conditions, we use the temperature of the free stream $T_1 = 163\,\mathrm{K}$, giving $Z_{R-T} = 3.25$ for N_2 (extrapolated from Chernyi et al (2002)). One can consider that this value of Z_{R-T} is representative to the value for air, since $Z_{R-T} = 3.45$ for O_2 at 300 K. The rotational-translational relaxation time τ_{R-T} is given by

$$\tau_{R-T} = \tau_0 Z_{R-T}, \tag{21}$$

where $\tau_0 = 1/\nu_0$ is the mean time between a collision of the gas species. In our experimental conditions, the collision frequency is $\nu_0 = 1.325 \times 10^6\,\mathrm{s}^{-1}$ for air. The relaxation time between rotation and translation is then $\tau_{R-T} = 2.45\,\mu\mathrm{s}$, corresponding to a relaxation length of 1.25 mm for a free stream velocity of $U_1 = 511\,\mathrm{m{\cdot}s}^{-1}$. This relaxation length represents the minimal distance required downstream the nozzle exit to be sure that the rotational modes are in equilibrium with the translational ones. Since the flat plate is placed 174 mm downstream the nozzle exit (see Sect. 2.2), it is justified to use the measurement of T_{rot} to determine the macroscopic temperature (i.e., T_{tr}) above the model. For a temperature of 250 K, $\nu_0 = 3.744 \times 10^6\,\mathrm{s}^{-1}$ and $Z_{R-T} = 3.81$, giving a relaxation length of 0.52 mm. In addition, Lengrand (1974) verified that the gap between the rotational and translational temperatures was negligible in similar experimental conditions.

Another unfavorable effect could be expected when the rotational temperature is measured in experiments with such low pressure. Many authors observed indeed a deviation of the rotational population levels from the Boltzmann distribution. In this study, the very low density can induce a non-Boltzmann rotational distribution, meaning that the use of T_{rot} to estimate the gas temperature can be not relevant. To clarify this statement, the rarefaction parameter P introduced by Bird (1970) is calculated. The value of P is estimated at two locations: at the exit of the nozzle ($x = -174\,\mathrm{mm}$) and above the flat plate ($x = 17.5\,\mathrm{mm}$ and $z = 30\,\mathrm{mm}$). At these positions, the rarefaction parameter is equal to $P = 0.32$ and $P = 1.7 \times 10^{-3}$, respectively. According to the correlation established by Campargue et al (1984) between the rarefaction parameter and the rotational breakdown criterion, the rarefied conditions of this study doesn't affect the rotational population distribution, which obey to a Boltzmann distribution. For the two reference positions chosen, the rotational temperature can be determined from the rotational levels with $J < 50$ at the exit of the nozzle, and from any rotational quantum number J at the position above the flat plate.

In view of these preliminary verifications, the temperature of the gas above the cathode can be deduced from rotational temperature measurements carried out with optical emission spectroscopy (OES) (Menier et al, 2007; Léger et al, 2009). The rotational temperatures are determined from the $N_2(C\,^3\Pi_u^+\text{-}B\,^3\Pi_g^+)$ second positive system and the $N_2^+(B\,^2\Sigma_u^+\text{-}X\,^2\Sigma_g^+)$ first negative system at $\lambda = 337.14\,\mathrm{nm}$ and $\lambda = 390.4\,\mathrm{nm}$, respectively. The measurement position was in the middle of the cathode according to the span of the flat plate (i.e., $y = 0\,\mathrm{mm}$). Because the model was placed in the middle of the isentropic uniform core of the flow and the distribution of the surface temperature in the spanwise direction (i.e., along the Y-axis) is minute (see Sect. 2.3.3), the gradient in the line of sight was negligible, meaning that the temperature measured by OES was representative of the effective local temperature above the cathode.

The results show that the gas temperature deduced from the rotational temperature is weakly increased by the discharge. For instance, Léger et al (2009) showed that with a similar plasma discharge with I_{HV} ranging between 28 mA and 57 mA and for wall-normal positions ranging between $z = 8\,\mathrm{mm}$ and 20 mm, the flow temperature increases by merely 10 K (from 230 K to 240 K, with an error estimated at $\pm 10\,\mathrm{K}$). This result leads us to consider that the bulk heating contribution to the modification of the flow field above the flat plate is negligible. Lago et al (2008) confirmed this statement in showing, with a Direct Simulation Monte Carlo method applied to a similar setup, that the bulk heating is not a relevant process to consider in order to explain the flow field modifications induced by a plasma actuator. Their conclusions are supported by the fact that, for the type of plasma created by a glow discharge in a low density flow (i.e., this

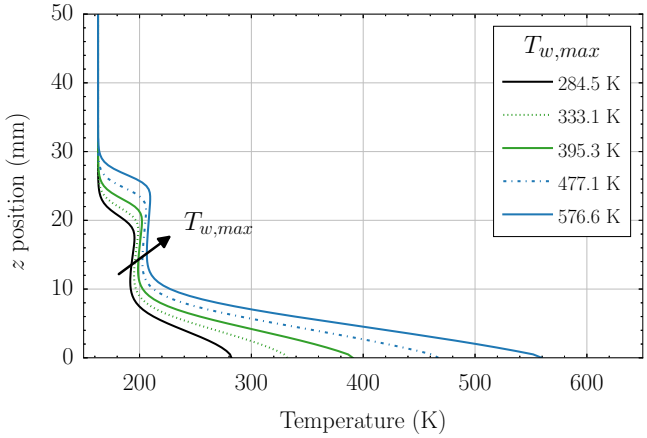

Fig. 17 Flow temperature profiles versus the wall-normal direction at $x = 17.5$ mm in the case of numerically simulated surface heating. The free stream Mach number is 2.

study), more than 90% of the total amount of input energy is stored into vibrational modes (Raizer, 1991), which relax on very long distances in a such type of flow (Lago et al, 2014).

Moreover, the temperature of the flow above the model surface can be determined from the numerical simulations (see Fig. 17). Because of the rarefied flow regime, the influence of surface heating is predominant close to the model surface. For wall-normal positions above $z = 10$ mm, bulk heating due to the heat source placed on the model surface is small. For an increase in the surface temperature of $\Delta T_w = 292.1$ K, the flow temperature at $z = 15$ mm is increased by $+12.6$ K. This result corroborates the fact that the bulk heating produced by the plasma actuator does not seem to play a significant role in the flow modification.

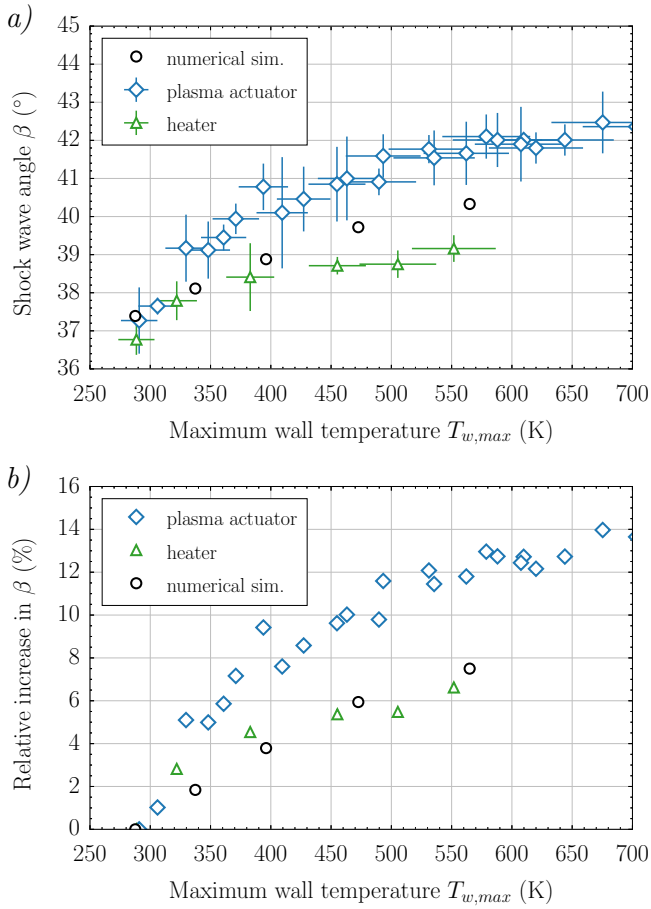

Fig. 18 Comparison of the shock wave angles measured with the two types of actuators (plasma actuator: diamonds; heater: triangles) and calculated with the numerical simulation (circles), in the case of: *(a)* absolute value of β and *(b)* relative increase in β with the baseline of each case taken as the reference. The free stream Mach number is 2.

6.3 Contribution of surface heating to the shock wave angle modification.

In order to differentiate the surface thermal effect from other types of effects (purely plasma effects, bulk heating), experiments were carried out using the heater as actuator. To analyze the effects induced by the heater, images of the flow field were recorded with the ICCD camera once thermal equilibrium had been reached. Analysis of the ICCD images shows that the thermal effect at the heater surface induces an increase in the shock wave angle (see Fig. 18, triangles) for all the operating conditions tested (with I_{HE} ranging between 0.4 A and 1.4 A). In Fig. 18, the shock wave angle β is plotted versus the maximum surface temperature $T_{w,max}$ to compare the measurements performed with the two types of actuators (plasma actuator and heater). The shock wave angle calculated with the numerical simulation is also reported in Fig. 18 (circles). Fig. 18a shows the absolute values of β. One can observe that the numerical simulation overestimates the shock wave angle for the baseline in comparison to the experimental devices (plasma actuator and heater). The values of β for the numerical simulation, corresponding to the cases of surface heating (i.e., $T_{w,max} > 300$ K), are therefore overestimated of the same difference. This was due to the earlier development of the inviscid layer (see Sect. 6.2). In order to compare the experimental devices with the numerical simulation, Fig. 18b shows the relative increase in β, in considering the baseline of each case as the reference to calculate the relative increase.

Using the heater instead of the plasma actuator induces similar shock wave modifications: the higher the surface temperature is, the higher the shock wave angle is; and the standoff distance remains within the 1–2 mm-range. However, for any given value of $T_{w,max}$, the shock wave angle measured with the heater is lower than the value estimated with the plasma actuator. This result is supported by the numerical simulation, which exhibits a relative increase in β similar to the one measured with the heater (see Fig. 18b). When the heating element is used, it is reasonable to assume that

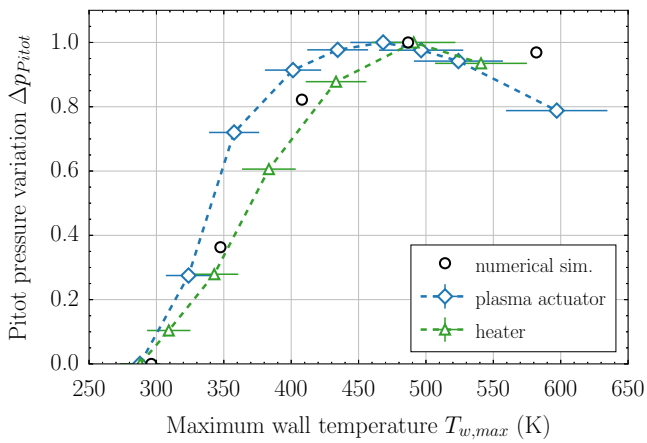

Fig. 19 Comparison of Pitot pressure increase measured with the two types of actuator (plasma actuator: diamonds; heater: triangles) and calculated with the numerical simulation (circles). The free stream Mach number is 2.

only a purely thermal effect at the model surface induces the flow modifications observed. In this case, the mechanism involved in the shock wave angle increase is the displacement effect (see Sect. 6.2). The experimental data presented in Fig. 18 provide a direct estimation of the surface heating effectiveness when the plasma actuator is used. The purely thermal effect at the flat plate surface therefore accounts for almost half of the total shock wave modification when the plasma actuator is used. Moreover, the contribution of surface heating to the shock wave modification decreases with the discharge current, meaning that the efficiency of other actuation modes in the shock wave modification increases. In this study, we chose to use the surface temperature instead of the power consumed by the actuators in order to compare them. The power consumed by the heater was indeed directly related to the wire resistivity because it depends on the wire diameter. This means that for two heaters made with wires of different resistance values, the power consumed can be significantly different between the heaters, even though the surface temperature remains the same. In addition, in the case of the plasma actuator, the input power applied to the discharge is distributed into heating, ionization, chemistry , while in the case of the heater all the consumed power is converted in heating. For these reasons, any deductions based on a comparison of the power consumed by the two actuators must be made in considering all the physical phenomena involved with the two types of actuators.

Analysis of the pressure variation at a constant wall-normal position (see Fig. 19) leads to the same conclusion as that obtained by estimating the shock wave angle optically. The wall-normal position $z = 17.5\,\text{mm}$ was chosen in order to measure 105% of the total pressure of the Mach 2 free stream, in the case of the baseline. The Pitot tube was therefore placed slightly above the shock wave. A pressure of $p_{Pitot,off} = 47.1\,\text{Pa}$ ($\approx 1.05 \times 44.9\,\text{Pa}$) was measured and taken as the reference to calculate the relative pressure variation Δp_{Pitot} when an actuator is used. This pressure variation is defined by

$$\Delta p_{Pitot} = \frac{p_{Pitot} - p_{Pitot,off}}{p_{Pitot,max} - p_{Pitot,off}}, \tag{22}$$

where p_{Pitot} is the Pitot pressure measured at $z = 17.5\,\text{mm}$, $p_{Pitot,off}$ is the Pitot pressure measured at $z = 17.5\,\text{mm}$ in the case of the baseline, and $p_{Pitot,max}$ is the maximum pressure of the Pitot profile measured at $x = 17.5\,\text{mm}$ in the case of the baseline (estimated with Fig. 16). At this particular wall-normal position, the displacement effect induced by the surface heating is responsible for an increase followed by a decrease in the Pitot pressure, whatever the actuation (plasma actuator or heater) was. However, the increase in Δp_{Pitot} in the case of the plasma actuator occurred at lower surface temperatures in comparison to the ones measured with a purely thermal effect (experimental or simulated heater). This result corroborates optical measurements and endorses the fact that other mechanisms than thermal ones (surface and bulk heating) must be considered to fully explain the observed shock wave modification by the plasma actuator, in particular those related to purely plasma properties.

Future work will be conducted to estimate the role played by the ionization rate, which is known to have the ability to significantly modify gas properties such as the isentropic exponent γ and, hence, the speed of sound (Burm et al, 1999). For this type of discharge (i.e., low pressure dc glow discharge), the simulations performed by Mahadevan and Raja (2010) showed that the highest values of charged species densities are reached in the vicinity of the plasma sheath. In our case, this result indicates that the ionization rate could have a sufficiently high level to modify the flow properties in the vicinity of the shock wave. Measurements of electronic properties (i.e., temperature and density) with a Langmuir probe will be conducted in order to quantify the level of the ionization rate. In particular, the positions upstream of the leading edge of the flat plate will be surveyed, since a necessary condition to achieve a noticeable plasma effect is to alter flow properties upstream the model (Kuo, 2007).

7 Conclusions

This work is focused on the quantification of surface heating when a shock wave is modified by a plasma actuator, in rarefied flow regime. It was experimentally observed that the increase in the surface temperature of the flat plate with the discharge current of the plasma actuator induces an increase in the shock wave angle. A heating element was therefore used instead of the plasma actuator in order to discriminate

purely surface heating from other types of effects. By measuring the flow modifications with optical and pressure devices for both actuators, it is now clear that surface heating is overlapped with purely plasma effects. Measurements showed that plasma effects become dominant over thermal effects with the discharge current. This study allows the magnitude of surface heating to be clearly determined when the plasma actuator is used. For the experimental setup studied in the present work, the purely thermal effect at the flat plate surface accounts for almost half of the total shock wave modification when the plasma actuator is used. Concerning the bulk heating induced by the dc glow discharge, previous works of our group lead us to consider that such a type of heating does not play a significant role in the modification of the slightly rarefied Mach 2 flow field above the flat plate.

In addition, numerical simulations were performed with a Navier-Stokes code modified with wall boundary conditions adapted to the slip-flow regime. The numerical simulation first enabled the flow field to be characterized without any actuator. Then, surface heating was achieved by modifying the boundary condition of the upper surface of the flat plate. Different temperature distributions were tested, corresponding to real experimental cases. Numerical simulations give results in good agreement with the experimental observations, thus confirming the conclusions drawn from the experiments.

Future improvements will be considered to better understand the coupling between the plasma and the flow. Experimentally, Langmuir probe measurements will be carried out over the flat plate to analyze the behavior of the electron density and temperature across the shock wave. These measurements will be coupled with optical spectroscopy measurements to investigate the non-thermal equilibrium properties which could have an influence on shock wave modifications.

Acknowledgements Romain Joussot's fellowship is provided by the French Government's Investissement d'Avenir program: Laboratoire d'Excellence CAPRYSSES (grant no. ANR-11-LABX-0006-01). Additional funding is provided by the Région Centre with the PASS grant (convention no. 00078782). The authors would like to acknowledge Dr. Ivan Fedioun for fruitful discussions. The authors would like to thank Daniel Andrieux (MPR Industries) for his technical assistance with the pumping group. The authors would furthermore like to acknowledge the constructive feedback from the reviewers.

References

Abernethy RB, Benedict RP, Dowdell RB (1985) ASME measurement uncertainty. J Fluid Eng-T ASME 107(2):161–4

Allègre J, Bisch C (1968) Angle of attack and leading edge effects on the flow about a flat plate at Mach number 18. AIAA J.6(5):848–52

Artana G, D'Adamo J, Léger L, Moreau E, Touchard G (2002) Flow control with electrohydrodynamic actuators. AIAA J.40(9):1773–9

Benard N, Mizuno A, Moreau E (2009) A large-scale multiple dielectric barrier discharge actuator based on an innovative three-electrode design. J. Phys. D: Appl. Phys.42(23):235,204 (12 pp.)

Bird GA (1970) Breakdown of translational and rotational equilibrium in gaseous expansions. AIAA J.8(11):1998–2003

Bityurin VA, Klimov AI (2005) Non-thermal plasma aerodynamics effects. In: AIAA Paper No. 2005–978

Bletzinger P, Ganguly BN, van Wie D, Garscadden A (2005) Plasmas in high speed aerodynamics. J. Phys. D: Appl. Phys.38(4):R33–57

Burm KTAL, Goedheer WJ, Schram DC (1999) The isentropic exponent in plasmas. Phys. Plasmas6(6):2622–7

Campargue R, Gaveau MA, Lebehot A (1984) Internal state populations in supersonic free jets and molecular beams. In: Rarefied Gas Dynamics, Proceedings of the 14th International Symposium, edited by H. Oguchi, Tokyo University Press, Tokyo, 1984, Vol. II, pp. 551-66

Chernyi GG, Losev SA, Macheret SO, Potapkin BV (2002) Physical and chemical processes in gas dynamics: cross sections and rate constants for physical and chemical processes, Volume 1. Progress in Astronautics & Aeronautics, Vol. 196, American Institute for Aeronautics and Astronautics

Dedrick J, Boswell RW, Audier P, Rabat H, Hong D, Charles C (2011) Plasma propagation of a 13.56 MHz asymmetric surface barrier discharge in atmospheric pressure air. J. Phys. D: Appl. Phys.44(20):205,202 (8 pp.)

Fisher SS, Bharathan D (1973) Glow-discharge flow visualization in low-density free jets. J. Spacecraft Rockets10(10):658–62

Fomin VM, Tretyakov PK, Taran JP (2004) Flow control using various plasma and aerodynamics approaches (short review). Aerosp Sci Technol 8(5):411–21

Gnemmi P, Rey C (2009) Plasma actuation for the control of a supersonic projectile. J. Spacecraft Rockets46(5):989–98

Hunter JD (2007) Matplotlib: A 2D graphics environment. Comput Sci Eng 9(3):90–5

Joussot R, Hong D, Rabat H, Boucinha V, Weber-Rozenbaum R, Leroy-Chesneau A (2010) Thermal characterization of a DBD plasma actuator: Dielectric temperature measurements using infrared thermography. In: AIAA Paper No. 2010-5102

Joussot R, Leroy A, Weber R, Rabat H, Loyer S, Hong D (2013) Plasma morphology and induced airflow characterization of a DBD actuator with serrated electrode. J. Phys. D: Appl. Phys.46(12):125,204 (12 pp.)

Kline SJ, McClintock FA (1953) Describing uncertainties in single-sample experiments. Mech Eng 75(1):3–8

Kogan MN (1969) Rarefied Gas Dynamics. Plenum Press, New York

Kuo SP (2007) Plasma mitigation of shock wave: experiments and theory. Shock Waves 17(4):225–39

Lago V, Lengrand JC, Menier E, Elizarova TG, Khokhlov AA (2008) Physical interpretation of the influence of a DC discharge on a supersonic rarefied flow over a flat plate. AIP Conf Proc 1084(1):901–906

Lago V, Joussot R, Parisse JD (2014) Influence of the ionization rate of a plasma discharge applied to the modification of a supersonic low reynolds number flow field around a cylinder. J. Phys. D: Appl. Phys.47(12):125,202 (13 pp.)

Léger L, Depussay E, Lago V (2009) D. C. surface discharge characteristics in Mach 2 rarefied airflow. IEEE T Dielect El In 16(2):396–403

Lengrand JC (1974) Mesure des températures de rotation dans l'azote à basse densité par sonde à faisceau électronique. application à l'étude des écoulements. PhD thesis, Université Paris VI, France

Leonov SB (2011) Review of plasma-based methods for high-speed flow control. AIP Conf Proc 1376:498–502

Leonov SB, Yarantsev DA (2008) Near-surface electrical discharge in supersonic airflow: Properties and flow control. J. Propul. Power24(6):1168–81

Macheret SO, Shneider MN, Miles RB (2004) Magnetohydrodynamic and electrohydrodynamic control of hypersonic flows of weakly ionized plasma. AIAA J.42(7):1378–87

Mahadevan S, Raja LL (2010) Simulations of direct-current air glow discharge at pressures ~ 1 Torr: Discharge model validation. J. Appl. Phys.107(9):093,304 (11 pp.)

Markelov GN, Kudryavtsev AN, Ivanov MS (2000) Continuum and kinetic simulation of laminar separated flow at hypersonic speeds. J. Spacecraft Rockets37(4):499–506

McCroskey WJ, Bogdonoff SM, McDougall JG (1966) An experimental model for the sharp flat plate in rarefied hypersonic flow. AIAA J.4(9):1580–7

Menier E (2007) Influence d'une décharge électrique continue sur un écoulement supersonique raréfié. PhD thesis, Université d'Orléans, France

Menier E, Lengrand JC, Depussay E, Lago V, Leger L (2006) Direct Simulation Monte Carlo method applied to the ionic wind in supersonic rarefied conditions. In: AIAA Paper No. 2006–3343

Menier E, Leger L, Depussay E, Lago V, Artana G (2007) Effect of a dc discharge on the supersonic rarefied air flow over a flat plate. J. Phys. D: Appl. Phys.40(3):695–701

Minkina W, Dudzik S (2009) Infrared Thermography: Errors and Uncertainties. John Wiley & Sons Ltd, Chichester, United Kingdom

Oliphant TE (2007) Python for scientific computing. Comput Sci Eng 9(3):10–20

Parisse JD, Léger L, Depussay E, Lago V, Burtschell Y (2009) Comparison between Mach 2 rarefied airflow modification by an electrical discharge and numerical simulation of airflow modification by surface heating. Phys. Fluids21(10):106,103 (9 pp.)

Raizer YP (1991) Gas discharge Physics. Springer-Verlag, Berlin Heidelberg

Roth JR (2003) Aerodynamic flow acceleration using paraelectric and peristaltic electrohydrodynamic effects of a one atmosphere uniform glow discharge plasma. Phys. Plasmas10(5):2117–26

Schneider CA, Rasband WS, Eliceiri KW (2012) NIH Image to ImageJ: 25 years of image analysis. Nat Methods 9(7):671–5

Semenov VE, Bondarenko VG, Gildenburg VB, Gubchenko VM, Smirnov AI (2002) Weakly ionized plasmas in aerospace applications. Plasma Phys. Contr. F.44(12B):B293–305

Shang JS, Kimmel RL, Menart J, Surzhikov ST (2008) Hypersonic flow control using surface plasma actuator. J. Propul. Power24(5):923–34

Shin J, Narayanaswamy V, Raja L, Clemens NT (2007) Characterization of a direct-current glow discharge plasma actuator in low-pressure supersonic flow. AIAA J.45(7):1596–605

Springer GS (1971) Heat transfer in rarefied gas. In: Irvine TF, Hartnett JP (eds) Advances in Heat Transfer, Vol. 7, pp.163–218, Academic Press, Inc., New York

Terlouw JP, Vogelaar MGR (2012) Kapteyn Package, version 2.2. Kapteyn Astronomical Institute, University of Groningen, The Netherlands, available from http://www.astro.rug.nl/software/kapteyn/

Wang L, Luo ZB, Xia ZX, Liu B, Deng X (2012) Review of actuators for high speed active flow control. Sci China Tech Sci 55(8):2225–40